Electronic supplementary information

Underlying potential evaluation of the real-process applications of magnetic porous liquids

Hamidreza Mahdavi,[a] Muhammad M. Sadiq,[a] Stefan J. D. Smith,[*a,b] Xavier Mulet,[*a,b] and Matthew R. Hill,[*a,b]

[a.] Department of Chemical and Biological Engineering, Monash University, Clayton, VIC 3800, Australia

[b.] CSIRO Manufacturing, Private Bag 10, Clayton South, VIC 3169, Australia

S1: Chemicals

The materials were all used as received, with no further purification. The sodium acetate trihydrate ($CH_3COONa \cdot 3H_2O$), magnesium chloride hexahydrate ($MgCl_2 \cdot 6H_2O$), ferric chloride hexahydrate ($FeCl_3 \cdot 6H_2O$), polyethylene glycol (PEG, Mw = 4000), zinc nitrate hexahydrate ($Zn(NO_3)_2 \cdot 6H_2O$), imidazole, and benzimidazole were purchased from Sigma Aldrich. Solvents compromised of 1,3,5-triisopropylbenzene (TPB), N,N-dimethylformamide (DMF), ethanol (EtOH), and methanol (MeOH) used for the synthesis were of analytical grade, were also obtained from Sigma Aldrich.

S2: Synthesis

$MgFe_2O_4$

27 mmol $CH_3COONa \cdot 3H_2O$ with 2.5 mmol $MgCl_2.6H_2O$, and 5 mmol $FeCl_3.6H_2O$ were mixed, and 2.00 g of PEG was added to the solution to act as a surfactant. The mixture was homogenized using vigorous stirring and heated under reflux at 180 °C for 16 h. The black magnetic nanoparticles were separated magnetically after cooling and washed with distilled water and EtOH, each at least 3 times before being dried in a vacuum oven at 80 °C for 12 h.

ZIF-62

In a 250 mL round-bottom flask, 94.19 mmol of imidazole and 10.46 mmol of benzimidazole were dissolved in 150 mL of DMF. The resulting solution was stirred while 6.98 mmol of $Zn(NO_3)_2 \cdot 6H_2O$ was added, which then was placed at 130 °C under reflux for 96 hours. In the next step, the flask was cooled to ambient temperature and the nanoparticles were collected using a centrifuge. In the end, they were washed in DMF and MeOH at least three times before being dried in a vacuum oven at 100 °C for 12 h.

$MgFe_2O_4$@ZIF-62

13 mg $MgFe_2O_4$ was dispersed in 150 mL of DMF in a 250 mL single-neck round-bottom flask, followed by ultrasonication for 30 minutes. Then, 94.19 mmol of imidazole and 10.46 mmol of benzimidazole were dissolved in it. 6.98 mmol of $Zn(NO_3)_2 \cdot 6H_2O$ was added to the resulting solution under stirring. Then, it was placed under reflux at 130 °C for 96 hours. Subsequently, the flask was cooled to ambient temperature and magnetic framework composites (MFCs) were separated magnetically. At last, they were washed with DMF and MeOH, each at least 3 times before being dried in a vacuum oven at 100 °C for 12 h. The procedure for 13 mg MgFe2O4 was repeated with 39, and 78 mg $MgFe_2O_4$ to yield 1 %, 3 %, and 6 % $MgFe_2O_4$@ZIF-62, respectively.

S3: Solvent

In order to prepare a porous liquid (PL), TPB was selected as a solvent. Based on its hydrophobic chemistry and the likelihood of its being sterically excluded from the pores of the ZIF-62, the solvent was selected. The chosen solvent is shown in **Table S1**.

Table S1. Solvent properties including physiochemical properties and molecular shape.[1]

Chemical name	Abbreviation	Type	Shape	Chemical formula	Van der Waals diameter (Å)
1,3,5-Triisopropylbenzene	TPB	Hydrocarbon	Triangular	$C_6H_3[CH(CH_3)_2]_3$	9.06

S4: MFC-solvent combinations preparation

After the MFCs have been introduced to the solvent individually, they were sonicated for 30 minutes to achieve initial dispersion. MFCs were added to the solvent at different loadings of 1 wt.%, 2.5 wt.%, 5 wt.%, and 10 wt. %.

S5: Fourier-transform infrared spectroscopy (FTIR)

Fourier-transform infrared spectroscopy (FTIR) spectra were obtained using a Thermo Scientific Nicolet 6700 FTIR over the wavenumber range of 400 to 2000 cm-1. The ZIF-62's FTIR spectra displayed the characteristic peaks associated with its consisting groups. The C=C and C–H peaks appear at 1464 cm^{-1} and 745 cm^{-1}, respectively. They are associated with the benzene group in benzimidazole. The peak at 668 cm^{-1} reflects the presence of imidazole. The C–H peak at 958 cm^{-1} and 1070 cm^{-1} has been attributed to the benzimidazole off-plane bending and imidazole off-plane bending, respectively. The weak C-H bending peaks over the range of 2000-1650 cm^{-1} are ascribed to the aromatic compound.[2] The magnetic nanoparticles are at low concentrations, so their peaks are not visible in the MFCs
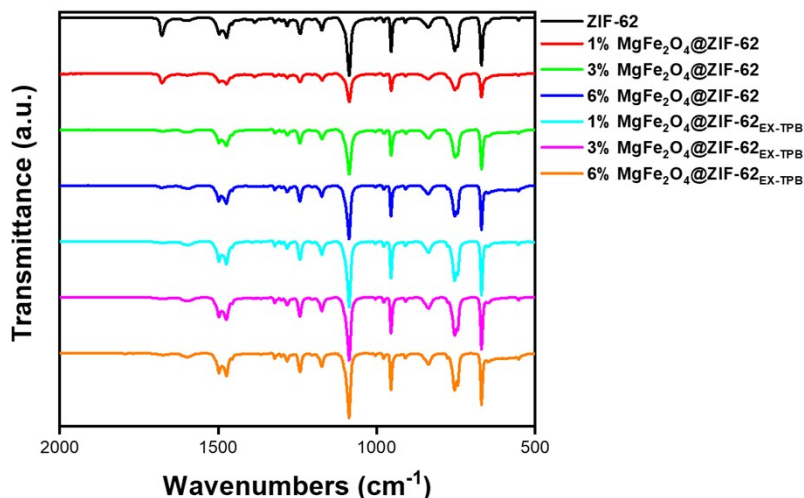

Figure S1. The structural group of ZIF-62 as control, and MFCs, and the effect of solvent exposure on structural groups through recovered MFCs containing different magnetic nanoparticles concentrations (1 wt. %, 3 wt. % and 6 wt. % of magnetic nanoparticles to ZIF-62 mass) using FTIR spectra.

S6. Powder X-ray diffraction (PXRD)

The powder X-ray Diffraction (PXRD) patterns were collected with a Bruker D8 Advance A25 XRD under Cu Kα radiation (40 kV, 40 mA). The samples were scanned at 0.02° step size and 1.6 seconds count time per step in the 2θ range of 5° to 45°. Samples were spun at a rate of 15 rpm during data collection. The ZIF-62's XRD pattern shows the correct phase structure and good crystallinity.[3] Since the magnetic nanoparticles are in low concentration, their peaks appear unobservable on the composite XRD.
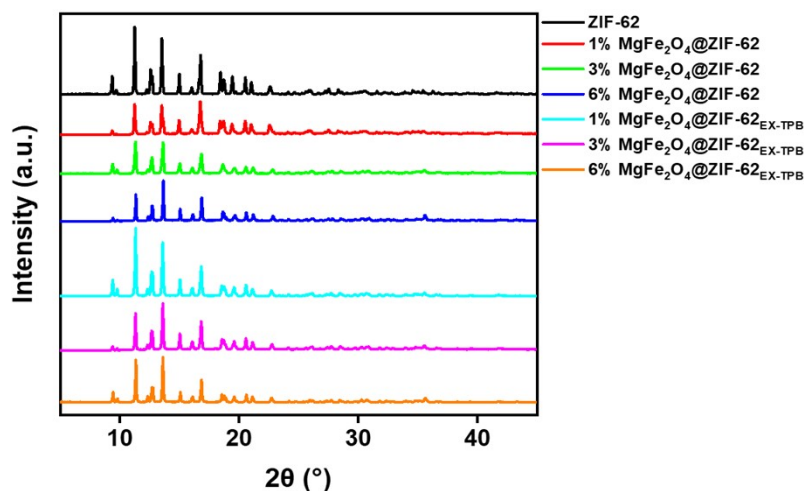

Figure S2. The crystal structure of ZIF-62 as control, and MFCs, and the effect of solvent exposure on crystal structure through recovered MFCs containing different magnetic nanoparticles concentrations (1 wt. %, 3 wt. % and 6 wt. % of magnetic nanoparticles to ZIF-62 mass) using PXRD patterns.

S7. Thermogravimetric analysis (TGA)

Thermogravimetric analysis (TGA) was performed in a controlled atmosphere using a Mettler Toledo TGA/SDTA851 analyzer to measure the changes in weight with temperature to determine thermal stability. The alumina crucibles were filled with samples and heated from 25 °C to 900 °C under a nitrogen atmosphere at a rate of 10 °C min^{-1}. Mass changes at the beginning of the analysis could be due to moisture adsorption or a loss of volatiles. The ZIF-62's TGA results demonstrate that the remaining solvent was removed around 200 °C, while common and typical bimodal degradation of the framework occurred at 350 °C and 650 °C, respectively.
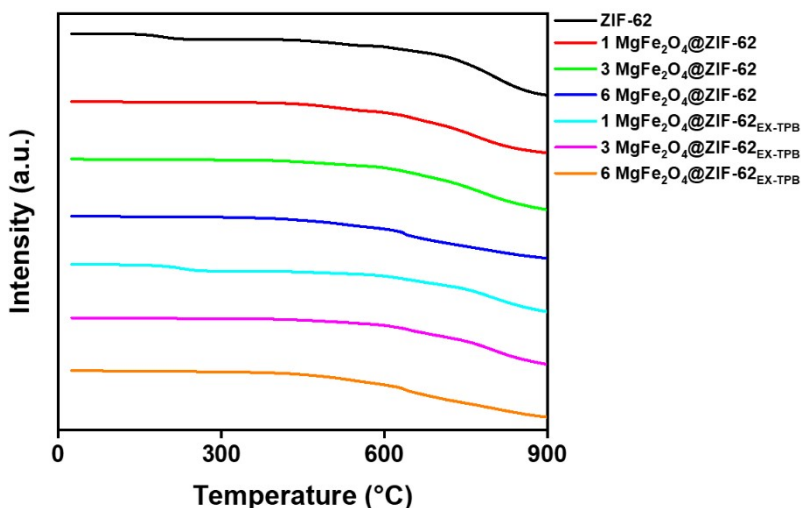

Figure S3. The thermal stability of ZIF62 as control, and MFCs, and the effect of solvent exposure on thermal stability through recovered MFCs containing different magnetic nanoparticles concentrations (1 wt. %, 3 wt. % and 6 wt. % of magnetic nanoparticles to ZIF-62 mass) using TGA.

S8. Low-pressure gas sorption

Micromeritics ASAP 2420 was used to determine the nitrogen adsorption isotherms at 77 K. Micromeritics software was used to calculate BET surface area and Langmuir surface area as well as the pore size distributions using the non-local density-functional theory (NLDFT) model with a slit pore geometry based on the collected isotherms. All the samples were activated under vacuum at 120 °C overnight. It was found that in ZIF-62 the low-pressure region exhibited a significant amount of adsorption, indicating that the microporosity was substantial. Whereas a minor amount of mesoporosity can be detected by the low degree of hysteresis between adsorption and desorption in high-pressure regions. Furthermore, microporous regions showed multiple peaks of pore sizes ranging from 6 Å and 12 Å, representing smaller tetrahedral and larger octahedral cavities.
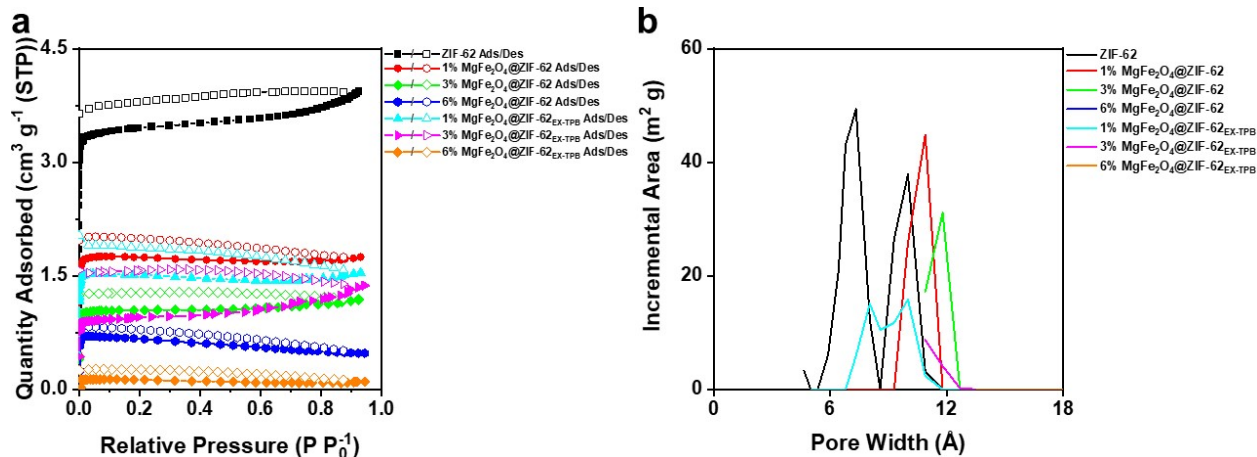

Figure S4. The N$_2$ adsorption isotherm and pore size distribution of ZIF-62 as control, and MFCs, and the effect of solvent exposure on N$_2$ adsorption isotherm and pore size distribution through recovered MFCs containing different magnetic nanoparticles

3

concentrations (1 wt. %, 3 wt. % and 6 wt. % of magnetic nanoparticles to ZIF-62 mass) using low-pressure gas sorption (adsorption is represented by filled markers and desorption by unfilled markers).

Table S2. The BET and Langmuir surface areas of ZIF-62 as control, and MFCs, and the effect of solvent exposure on BET and Langmuir surface areas through recovered MFCs containing different magnetic nanoparticles concentrations (1 wt. %, 3 wt. % and 6 wt. % of magnetic nanoparticles to ZIF-62 mass) using low-pressure gas sorption.

Sample	BET Surface Area ($m^2\,g^{-1}$)	Langmuir Surface Area ($m^2\,g^{-1}$)
ZIF-62	260	340
1% MgFe$_2$O$_4$@ZIF-62	130	170
3% MgFe$_2$O$_4$@ZIF-62	70	90
6% MgFe$_2$O$_4$@ZIF-62	50	60
1% MgFe$_2$O$_4$@ZIF-62$_{EX\text{-}TPB}$	110	150
3% MgFe$_2$O$_4$@ZIF-62$_{EX\text{-}TPB}$	80	100
6% MgFe$_2$O$_4$@ZIF-62$_{EX\text{-}TPB}$	10	12

S9. Scanning electron microscopy (SEM)

The scanning electron microscope (SEM) images of the samples were captured using an FEI Nova Nano scanning emission electron microscope with an accelerating voltage of 5 kV. As can be seen from the SEM image, the ZIF-62 was well-synthesised with morphology that confirm mesoscale order. According to the SEM images, the morphology of MFCs remained unchanged.
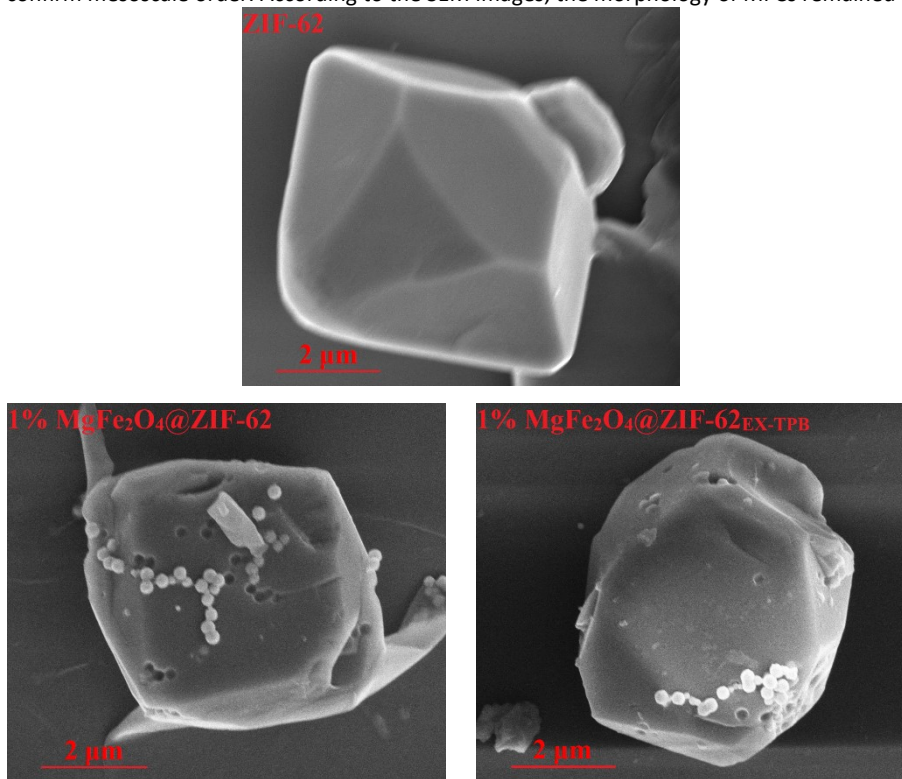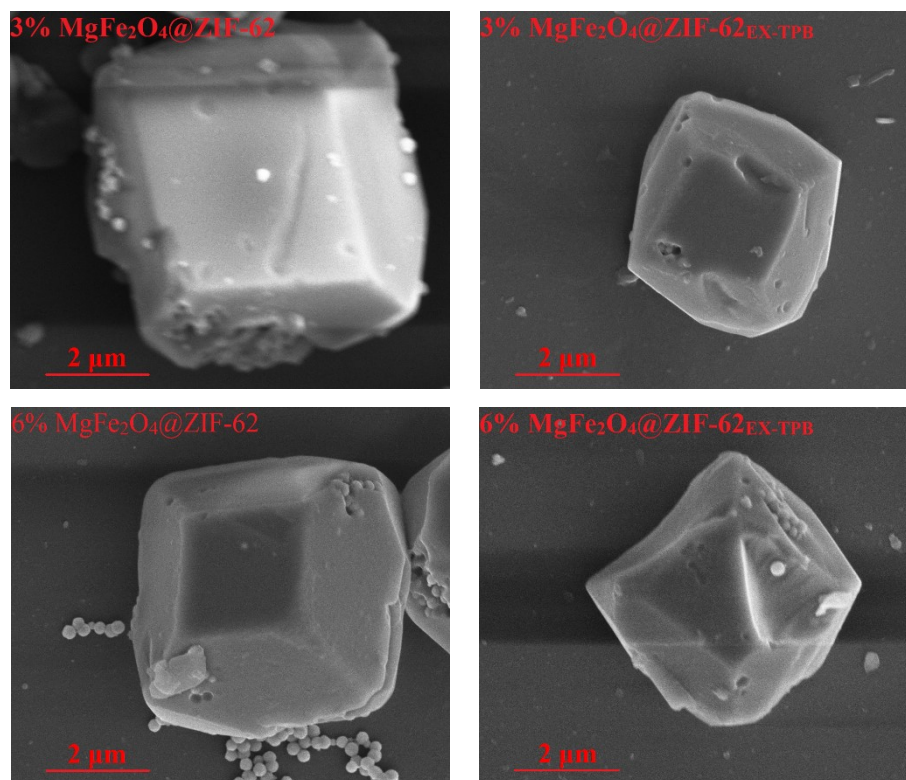
Figure S5. The morphology and size of ZIF-62 as control, and MFCs, and the effect of solvent exposure on morphology and size through recovered MFCs containing different magnetic nanoparticles concentrations (1 wt. %, 3 wt. % and 6 wt. % of magnetic nanoparticles to ZIF-62 mass) using SEM images.

S10. Vibrating sample magnetometer (VSM)

Magnetization curves (hysteresis loops), as well as saturation magnetization values were obtained by a vibrating sample magnetometer (VSM, RIKEN DENSHI). The powder samples were sealed in epoxy resin in a cylindrical sample holder in order to make the measurement, which was then allowed to be set and dry before being analyzed. The experiment was conducted with a maximum field of 10 kOe at room temperature. A negative susceptibility is seen in ZIF-62's magnetization curve, reflecting its diamagnetism. Whereas, MFCs show a spontaneous magnetization and their high Ms values can be attributed to the dry powders' ability to heat up quickly upon being exposed to an ac magnetic field.
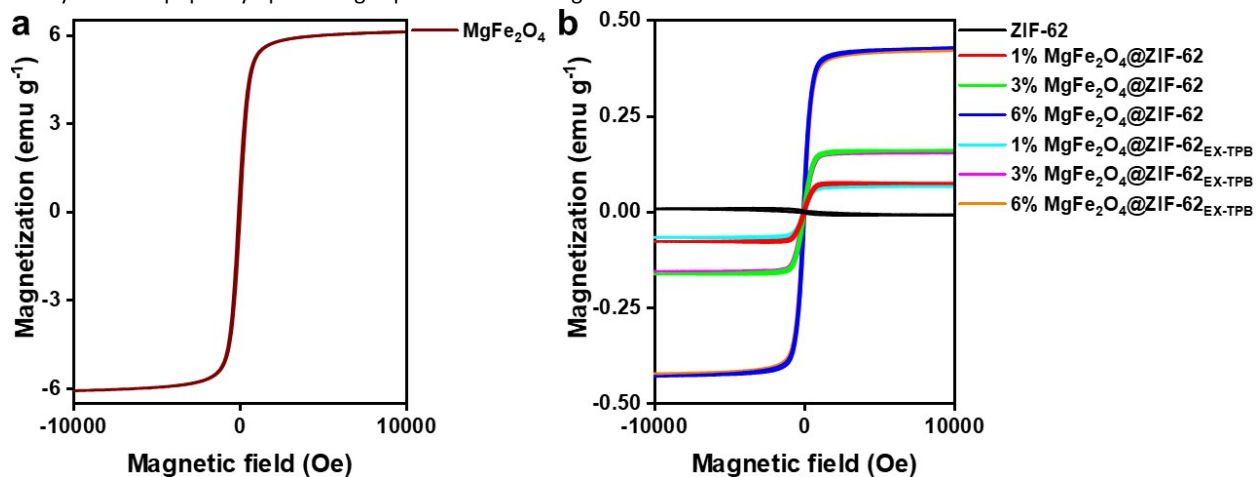

Figure S6. Hysteresis loops of a) $MgFe_2O_4$ as control, and b) ZIF-62 as control, and MFCs, and the effect of solvent exposure on hysteresis loops through recovered MFCs containing different magnetic nanoparticles concentrations (1 wt. %, 3 wt. % and 6 wt.

% of magnetic nanoparticles to ZIF-62 mass) using VSM.

Table S3. Saturation magnetization (Ms) values of $MgFe_2O_4$, ZIF-62 as controls, and MFCs, and the effect of solvent exposure on Ms through recovered MFCs containing different magnetic nanoparticles concentrations (1 wt. %, 3 wt. % and 6 wt. % of magnetic nanoparticles to ZIF-62 mass) using VSM.

MOFs	Ms (emu g^{-1})
$MgFe_2O_4$	0.4209
ZIF-62	-0.0101
1% $MgFe_2O_4$@ZIF-62	0.0729
3% $MgFe_2O_4$@ZIF-62	0.1590
6% $MgFe_2O_4$@ZIF-62	0.4274
1% $MgFe_2O_4$@ZIF-62$_{EX-TPB}$	0.0650
3% $MgFe_2O_4$@ZIF-62$_{EX-TPB}$	0.1525
6% $MgFe_2O_4$@ZIF-62$_{EX-TPB}$	0.4209

S 11. Inductive coupled plasma (ICP)

The magnetic nanoparticle content of the MFCs was analyzed using inductive coupled plasma (ICP) analysis by Agilent 5900 ICP-OES Anton Paar Multiwave 7000. Anton Paar Multiwave 7000 microwave digestion unit was used to digest samples with 69% HNO_3. Digest solutions were prepared in volumetric flasks and diluted according to requirements, before being analyzed by ICP-OES for desired elements. A certified multi-element standard was used to validate the calibrations and to check the method used.

Table S5. Elemental composition of $MgFe_2O_4$, and ZIF-62 as controls, and MFCs, and the effect of solvent exposure on elemental composition through recovered MFCs containing different magnetic nanoparticles concentrations (1 wt. %, 3 wt. % and 6 wt. % of magnetic nanoparticles to ZIF-62 mass) using ICP.

Sample	Atomic %		
	Zn	Mg	Fe
$MgFe_2O_4$	0.03	1.57	62.2
ZIF-62	30.1	---	---
1% $MgFe_2O_4$@ZIF-62	27.8	0.01	0.37
3% $MgFe_2O_4$@ZIF-62	29.1	0.04	1.73
6% $MgFe_2O_4$@ZIF-62	27.3	0.12	5.30
1% $MgFe_2O_4$@ZIF-62$_{EX-TPB}$	30.2	0.02	0.90
3% $MgFe_2O_4$@ZIF-62$_{EX-TPB}$	30.1	0.02	1.12
6% $MgFe_2O_4$@ZIF-62$_{EX-TPB}$	27.5	0.11	4.99

S12. X-ray photoelectron spectroscopy (XPS)

X-ray photoelectron spectroscopy (XPS) measurements were carried out on a Thermo Nexsa Surface Analysis System. It was equipped with a monochromatic Al Kα X-ray source (1486.6 eV), powered by 144 W 72 W (6 mA × 12 kV). Corrections to the core level binding energies were made using the C 1s binding energy of 284.8 eV. The spot size or area for analysis was 400 um^2 or 400 × 800 μm^2. Avantage software version 5 was used to process the data. Incorporating integral peak intensities with the sensitivity factors provided by the manufacturer was used to calculate atomic concentrations for all elements using survey spectra. The ZIF-62's XPS results, including the binding energies and atomic percentages of zinc, carbon, and nitrogen were consistent with the energy levels reported in the literature, which confirms successful syntheses. ZIF-62 showed some oxygen, which may have been due to moisture adsorbed. In addition, because XPS provides information about the surface composition, it is natural for magnesium, iron, and oxygen to be detected due to the presence of magnetic nanoparticles incorporated in MFCs.[4]
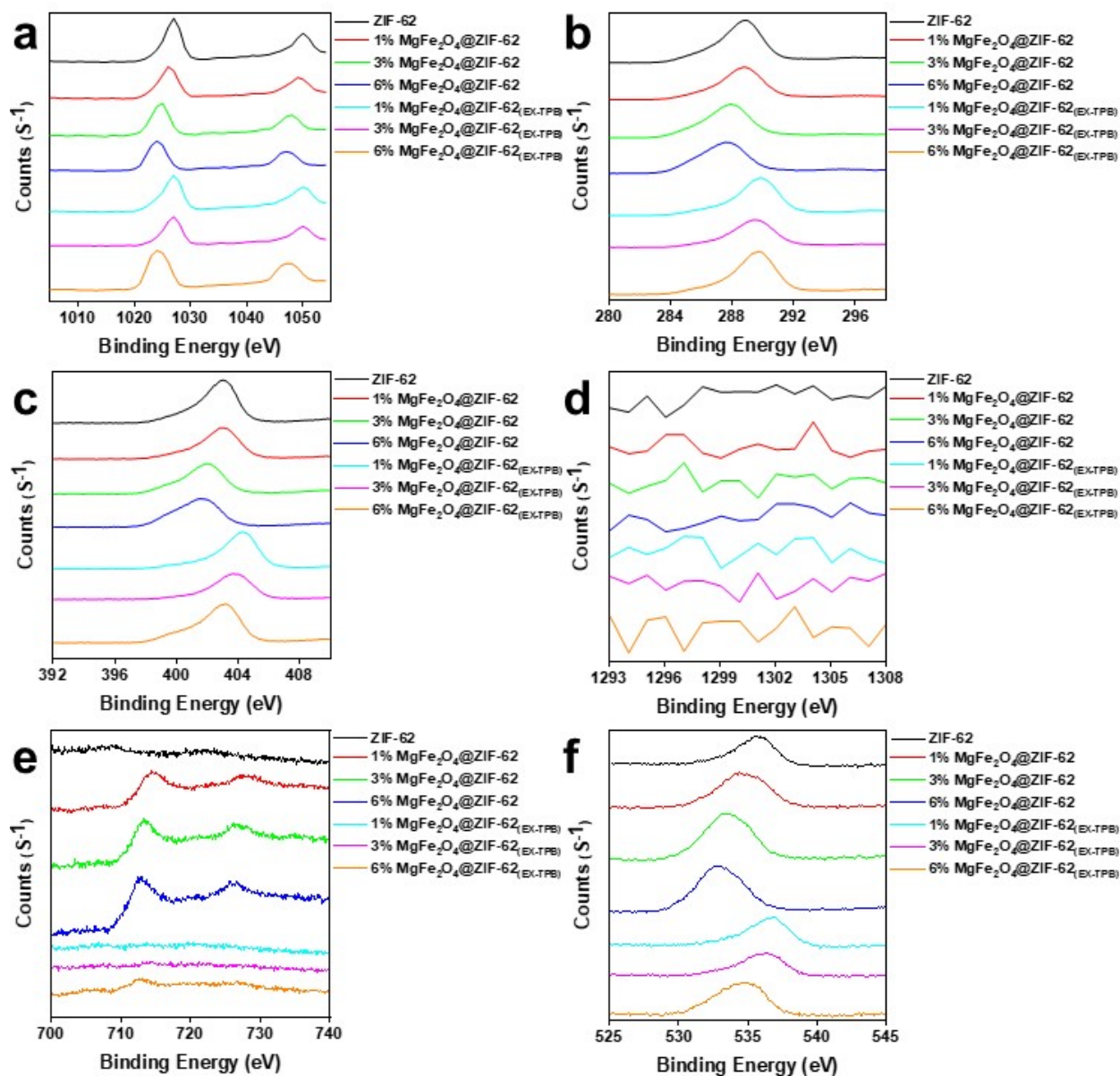
Figure S7. Binding energy levels of a) zinc 2p, b) carbon 1s, c) nitrogen 1s, d) magnesium 1s, e) iron 2p, and f) oxygen 1s of ZIF-62 as control, and MFCs, and the effect of solvent exposure on binding energy through recovered MFCs containing different magnetic nanoparticles concentrations (1 wt. %, 3 wt. % and 6 wt. % of magnetic nanoparticles to ZIF-62 mass) using XPS.

Table S5. Elemental composition of ZIF-62 as control, and MFCs, and the effect of solvent exposure on elemental composition through recovered MFCs containing different magnetic nanoparticles concentrations (1 wt. %, 3 wt. % and 6 wt. % of magnetic nanoparticles to ZIF-62 mass) using XPS.

Sample	Atomic %					
	Zn	C	N	Mg	Fe	O
ZIF-62	7.4	59.35	27.24	---	---	5.36
1% MgFe$_2$O$_4$@ZIF-62	7.58	58.55	26.41	0.08	0.05	7.15
3% MgFe$_2$O$_4$@ZIF-62	7.53	58.69	25.49	0.09	0.06	7.6
6% MgFe$_2$O$_4$@ZIF-62	7.39	59.33	26.05	0.1	0.07	7.07

1% MgFe$_2$O$_4$@ZIF-62$_{EX-TPB}$	7	57.04	26.21	0.11	0.06	9.51
3% MgFe$_2$O$_4$@ZIF-62$_{EX-TPB}$	6.52	57.51	24.47	0.1	0.07	11.51
6% MgFe$_2$O$_4$@ZIF-62$_{EX-TPB}$	6.06	55.54	24.63	0.13	0.08	11.83

S13. Solid-state nuclear magnetic resonance (^{13}C NMR)

Solid-State Nuclear Magnetic Resonance (^{13}C NMR) spectra were collected using a Bruker Avance III 500MHz spectrometer equipped with a 4 mm MAS probe (125.77 MHz for ^{13}C, 500.13 MHz for ^{1}H). The signals that belong to the different C sites of benzimidazole and imidazole in crystalline ZIF-62 have been determined. The results are in agreement with the literature.[5] NMR is not able to detect the magnetic nanoparticle signals on the composite because the nanoparticles are in low concentration.
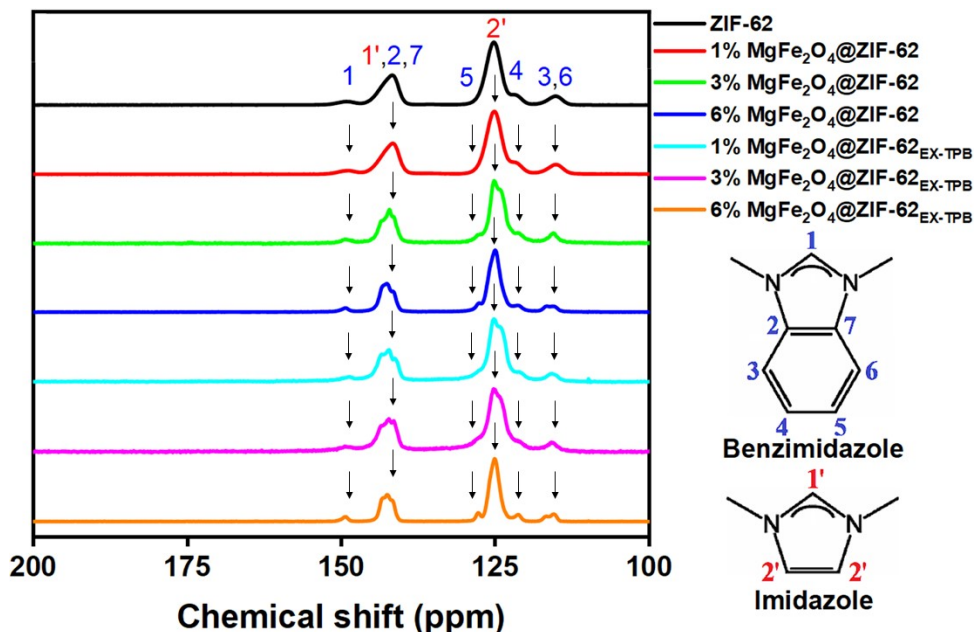

Figure S8. The chemical structure of ZIF-62 as control, and MFCs, and the effect of solvent exposure on chemical structure through recovered MFCs containing different magnetic nanoparticles concentrations (1 wt. %, 3 wt. % and 6 wt. % of magnetic nanoparticles to ZIF-62 mass) using ^{13}C NMR spectra.

S14: Fluidity properties

The viscosity of the samples was measured using the Anton-Paar Rheometer MCR 302. Samples were subjected to 20 measurements in sequence, and an average value was calculated for each sample. The viscosities of solvent and MPLs containing 10 wt % of MFC to solvent mass were measured.
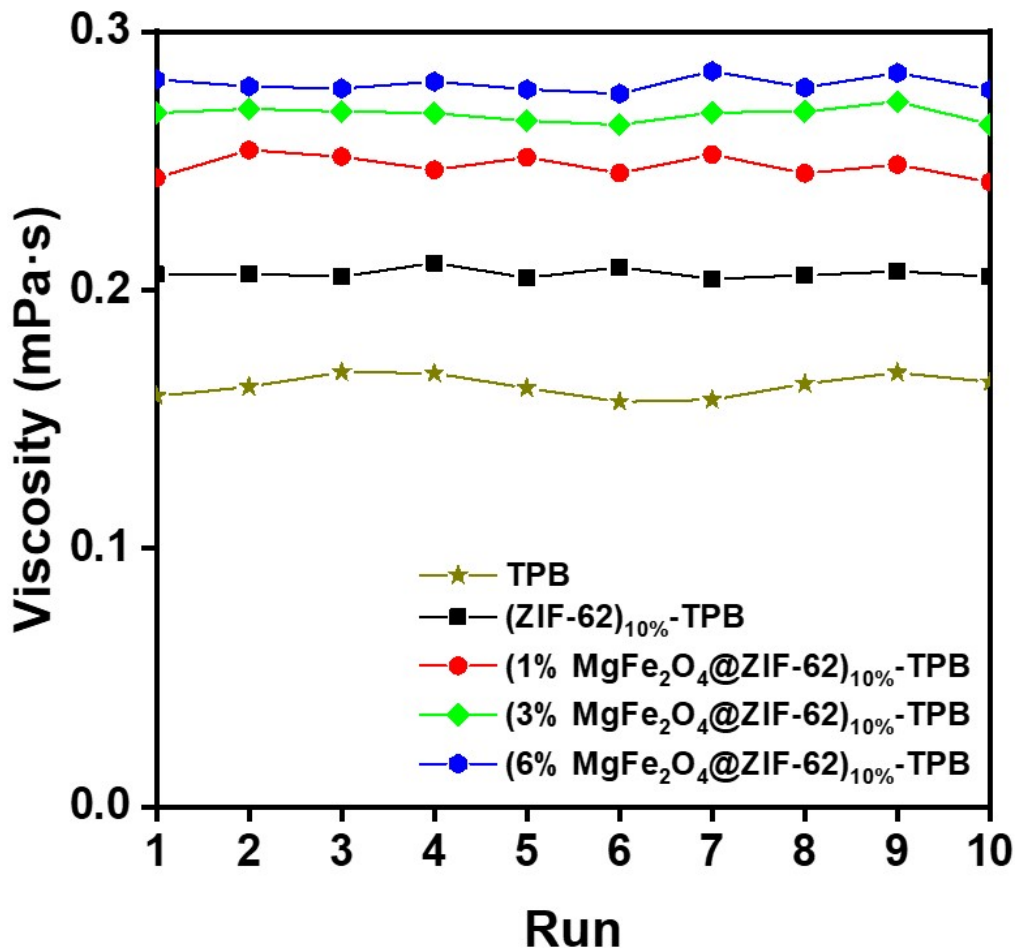
Figure S9. Measured viscosities of TPB, and (ZIF-62)$_{10\%}$-TPB as controls, and MPLs with 10 % MFCs containing different magnetic nanoparticles concentrations (1 wt. %, 3 wt. % and 6 wt. % of magnetic nanoparticles to ZIF-62 mass) compared to solvent.

Table S6. Average measured viscosities of TPB, and ZIF-62$_{10\%}$-TPB as controls, and MPLs with 10 % MFCs containing different magnetic nanoparticles concentrations (1 wt. %, 3 wt. % and 6 wt. % of magnetic nanoparticles to ZIF-62 mass) compared to solvent.

Sample	Viscosity (mPa s)	±	Difference between the solvent and MPL (%)
TPB	0.1630	0.0042	---
(ZIF-62)$_{10\%}$-TPB	0.2064	0.0019	26.6258
(1% MgFe$_2$O$_4$@ZIF-62)$_{10\%}$-TPB	0.2480	0.0042	52.1472
(3% MgFe$_2$O$_4$@ZIF-62)$_{10\%}$-TPB	0.2680	0.0028	64.4172
(6% MgFe$_2$O$_4$@ZIF-62)$_{10\%}$-TPB	0.2797	0.0029	71.5951

S15: Density

A Helium Pycnometer AccuPyc II 1340 was used to determine the skeletal or atomistic density of the sample according to the measured volume of known masses. The MFCs and solvent densities were determined. The MPLs' ideal densities were computed as perfect mixtures using solvent and MFCs atomic densities. Finally, MPLs density measurements were conducted.
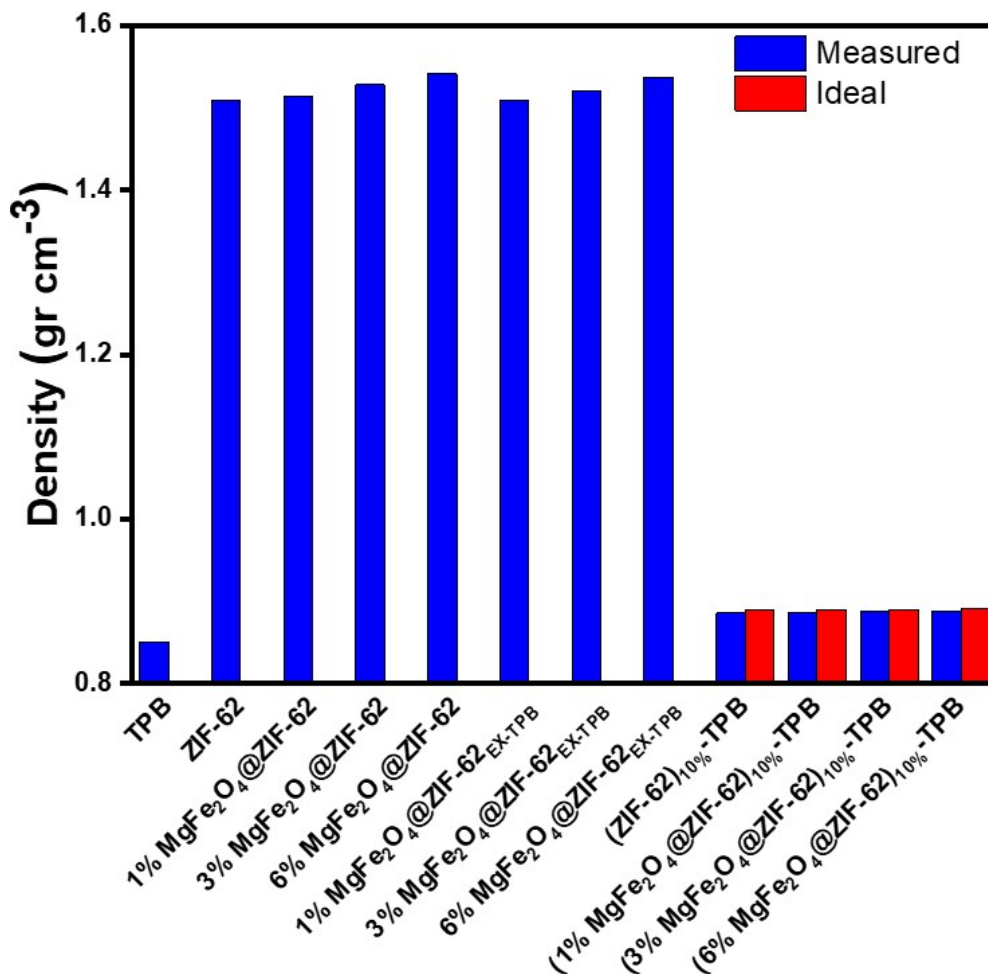
9

Figure S10. The Ideal and measured densities of TPB, ZIF-62, and (ZIF-62)$_{10\%}$-TPB as controls, and MFCs, and the effect of solvent exposure on densities through recovered MFCs and MPLs with 10 % MFCs containing different magnetic nanoparticles concentrations (1 wt. %, 3 wt. % and 6 wt. % of magnetic nanoparticles to ZIF-62 mass).

Table S7. The Ideal and measured densities of TPB, ZIF-62, and (ZIF-62)$_{10\%}$-TPB as controls, and MFCs, and the effect of solvent exposure on densities through recovered MFCs and MPLs with 10 % MFCs containing different magnetic nanoparticles concentrations (1 wt. %, 3 wt. % and 6 wt. % of magnetic nanoparticles to ZIF-62 mass).

Sample	Experimental density (g cm^{-3})	Calculation density (g cm^{-3})	Difference (%)
TPB	0.85067	--	--
ZIF-62	1.50864	--	--
1% MgFe$_2$O$_4$@ZIF-62	1.51465	--	--
3% MgFe$_2$O$_4$@ZIF-62	1.52798	--	--
6% MgFe$_2$O$_4$@ZIF-62	1.54139	--	--
1% MgFe$_2$O$_4$@ZIF-62$_{EX-TPB}$	1.50886	--	--
3% MgFe$_2$O$_4$@ZIF-62$_{EX-TPB}$	1.52011	--	--
6% MgFe$_2$O$_4$@ZIF-62$_{EX-TPB}$	1.53692	--	--
(ZIF-62)$_{10\%}$-TPB	0.88558	0.88946	0.388
(1% MgFe$_2$O$_4$@ZIF-62)$_{10\%}$-TPB	0.88664	0.88967	0.303
(3% MgFe$_2$O$_4$@ZIF-62)$_{10\%}$-TPB	0.88759	0.89013	0.254
(6% MgFe$_2$O$_4$@ZIF-62)$_{10\%}$-TPB	0.88843	0.89058	0.215

S16: High-pressure gas sorption

Gravimetric sorption isotherms were determined using an Intelligent Gravimetric Analyser (IGA-001) provided by HidenAnalytical (Ltd). High-pressure gas sorption experiments were conducted using pure CO_2 gas. The pressure was measured with an accurate pressure transducer, and the temperature was maintained with a Grant refrigerator maintained at 298 K with an accuracy of 0.05 K. The control software automatically corrected buoyancy effects. Prior to sorption measurements, ZIF-62 and MFCs samples were in-situ activated for 5 h at 120 °C and under vacuum, while the partial vacuum was used for the solvent and MPLs. Thus, no guest molecules or vapours remained in the samples following in situ activation.
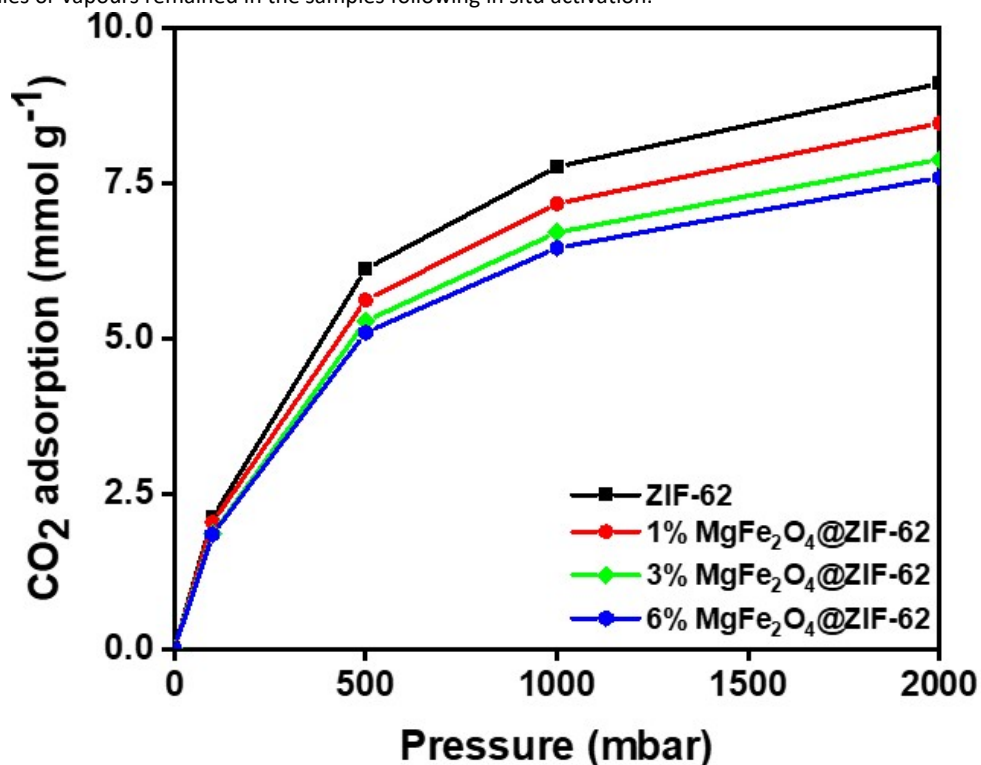

Figure S11.The CO_2 sorption capacity of ZIF-62 as control, and MFCs containing different magnetic nanoparticles concentrations (1 wt. %, 3 wt. % and 6 wt. % of magnetic nanoparticles to ZIF-62 mass) using pure CO_2 at 298 K.

S17: Static and dynamic gas sorption and desorption

The static and dynamic gas sorption and desorption breakthrough experiments were performed using a combination of an Ambrell induction heating machine and adsorption equipment. For this purpose, a mixed gas containing CO_2:N_2 by the composition of 15:85 v/v % was used. Furthermore, He gas as a common technique in gas separation processes was used as sweeping the desorbed gas. During sorption experiments, pressure and temperature were maintained at 1 atm and 298 K, respectively. A magnetic field provided by an induction heating machine with 160 amps was utilized for the desorption experiments. GasLab version 2.1 was used to record the data provided by ExplorIR®-W 100% CO_2 sensor. Before preparing MPLs samples for sorption measurements, ZIF-62 and MFCs samples were activated ex-situ for 5 h at 120 °C under vacuum. Therefore, no guest vapours or molecules remained in the samples after ex-situ activation.
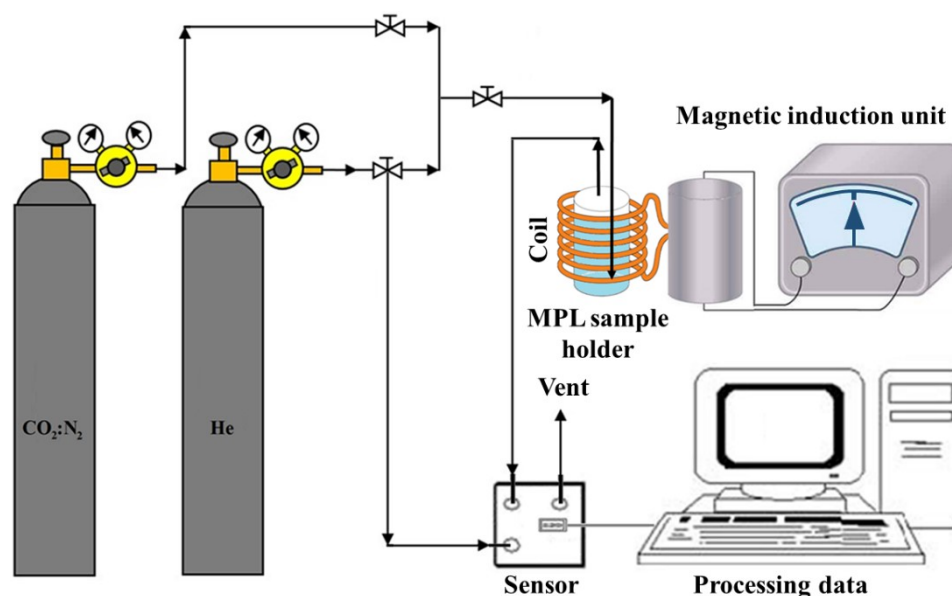
Figure S12.The combination of an induction heating machine and adsorption equipment.

Table S8. The static gas sorption, and desorption breakthrough and CO_2 removal results of TPB, and $(ZIF-62)_{10\%}$-TPB as controls, and MPLs with 10 % MFCs containing different magnetic nanoparticles concentrations (1 wt. %, 3 wt. % and 6 wt. % of magnetic nanoparticles to ZIF-62 mass) using mixed gas $CO_2:N_2$ (15:85, v/v %) at 298 K.

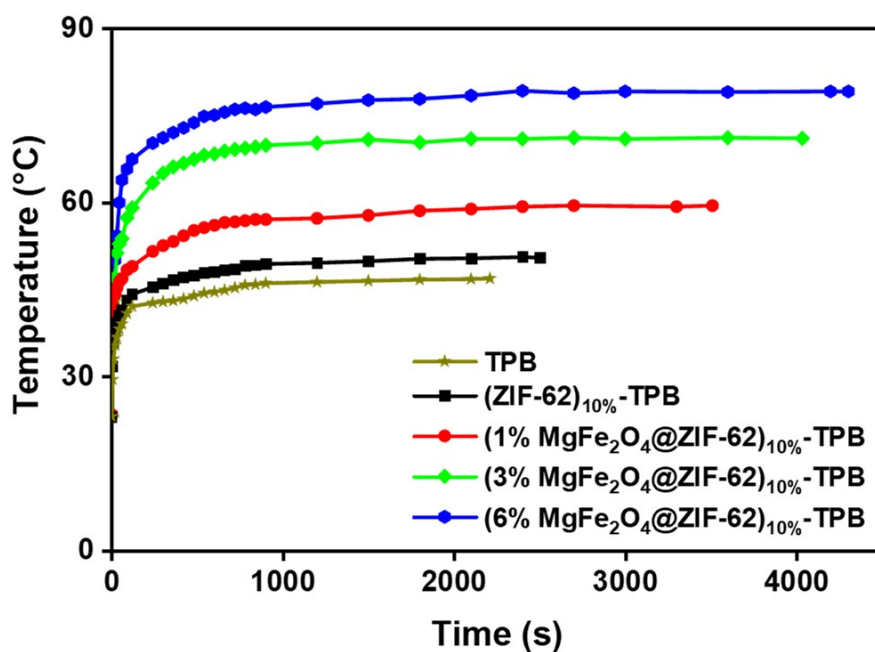| Sample	Sorption (mg)	Desorption (mg)	CO_2 removal (%)
TPB	3.25	1.57	48.38
$(ZIF-62)_{10\%}$-TPB	6.03	1.83	30.32
$(1\% \ MgFe_2O_4@ZIF-62)_{10\%}$-TPB	5.31	2.41	45.31
$(3\% \ MgFe_2O_4@ZIF-62)_{10\%}$-TPB	4.84	3.14	64.82
$(6\% \ MgFe_2O_4@ZIF-62)_{10\%}$-TPB	4.27	3.28	76.86

Figure S13.The samples' temperature as a function of time during static gas desorption breakthrough.

Table S9. The dynamic gas sorption, and desorption breakthrough and CO_2 removal results of (3% $MgFe_2O_4$@ZIF-62)$_{10\%}$-TPB using mixed gas CO_2:N_2 (15:85, v/v %) at 298.

Sample	Adsorption (mg)	Desorption (mg)	CO_2 removal (%)
(3% $MgFe_2O_4$@ZIF-62)$_{10\%}$-TPB Cycle 1	4.84	3.14	64.82
(3% $MgFe_2O_4$@ZIF-62)$_{10\%}$-TPB Cycle 2	4.98	3.07	61.57
(3% $MgFe_2O_4$@ZIF-62)$_{10\%}$-TPB Cycle 3	5.01	2.87	57.29

S17: Energy-Efficient MPL Regeneration

The desorption energy for each regeneration cycle is calculated by multiplying the mass of MPL by its specific heat capacity by the regeneration temperature difference using **Figure S13**.[5-7] Productivity is determined by dividing the quantity of CO_2 produced by the sum of the CO_2 produced and the mass of the MPL, divided by the time taken for regeneration. The regeneration energy of MPL is calculated by dividing the desorption energy for each regeneration cycle by the cumulative mass of CO_2 produced during each regeneration cycle. The energy consumption is determined similarly to regeneration energy, but in kilowatt-hours (kWh), which is more applicable to real-world terms.[8, 9]

Table S10. The desorption energy, productivity, regeneration energy, and energy consumption results of (3% $MgFe_2O_4$@ZIF-62)$_{10\%}$-TPB using mixed gas CO_2:N_2 (15:85, v/v %).

Sample	Desorption energy (J)	Regeneration energy (MJ kg CO_2^{-1})	Productivity (kgCO_2 h^{-1} kgMPL^{-1})	Energy consumption (KWh kgCO_2^{-1})
(3% $MgFe_2O_4$@ZIF-62)$_{10\%}$-TPB Cycle 1	869.59	0.2771	0.2800	0.0770
(3% $MgFe_2O_4$@ZIF-62)$_{10\%}$-TPB Cycle 2	869.59	0.2834	0.2786	0.0787
(3% $MgFe_2O_4$@ZIF-62)$_{10\%}$-TPB Cycle 3	869.59	0.3032	0.2779	0.0842

Desorption energy (J) = $\sum (m_i Cp_{ave,i} \Delta T)$ (Eq. 1)
Productivity (kgCO_2 h^{-1} kgAds^{-1}) = (Desorbed CO_2 mass)/(Desorption time × Adsorbate mass)   (Eq. 2)
Regeneration energy (MJ kgCO_2^{-1}) = Desorption energy/Desorbed CO_2 mass   (Eq. 3)
Energy consumption (KWh kgCO_2^{-1}) = Consumption energy/Desorbed CO_2 mass   (Eq. 4)

Author Contributions

H. M. led the project administration, conceptual and experimental design, analysis, interpretation of results, and writing of the draft. M.M.S., S.J.D.S., X.M., and M.R.H. contributed to the project administration, conceptual and experimental design, analysis, and interpretation of results.

References

1. H. Mahdavi, J. Burdloff, A. Robin, S. J. D. Smith, X. Mulet and M. R. Hill, *ACS Mater. Lett.*, 2023, **5**, 549-557.
2. G. Khandelwal, N. P. Maria Joseph Raj and S.-J. Kim, *J. Mater. Chem. A*, 2020, **8**, 17817-17825.
3. H. Mahdavi, H. Zhang, L. K. Macreadie, C. M. Doherty, D. Acharya, S. J. D. Smith, X. Mulet and M. R. Hill, *Nano Res.*, 2022, **15**, 3533-3538.
4. A. K. N S, A. S and P. M, *Mater. Res. Express*, 2019, **6**, 125049.
5. A. Qiao, D. Bennett Thomas, H. Tao, A. Krajnc, G. Mali, M. Doherty Cara, W. Thornton Aaron, C. Mauro John, G. N. Greaves and Y. Yue, *Sci. Adv.*, **4**, eaao6827.
6. A. I. Turkin, V. A. Drebushchak, Y. A. Kovalevskaya and I. E. Paukov, *J. Therm. Anal. Calorim.*, 2008, **92**, 717-721.
7. K. G. Joback and R. C. Reid, *Chem. Eng. Commun.*, 1987, **57**, 233-243.
8. M. M. Sadiq, K. Konstas, P. Falcaro, A. J. Hill, K. Suzuki and M. R. Hill, *Cell Rep. Phys. Sci.*, 2020, **1**, 100070.
9. M. R. M. Abu-Zahra, J. P. M. Niederer, P. H. M. Feron and G. F. Versteeg, *Int. J. Greenhouse Gas Control*, 2007, **1**, 135-142.